

# Heuristic Analysis of Viscous Dissipation in Single-Screw Extrusion

Wolfgang Roland , Jürgen Miethlinger

Institute of Polymer Extrusion and Compounding, Johannes Kepler University Linz, Altenbergerstraße 69, Linz 4040, Austria

**Modeling the non-Newtonian flow of polymer melts in single-screw extrusion generally requires numerical methods. This study analyzes the viscous dissipation of the melt-conveying zone, which is mainly responsible for the axial melt temperature increase, in single-screw extruders for both one- and two-dimensional stationary, fully developed flows of a power-law fluid. Rewriting the flow equations and applying the theory of similarity revealed three independent parameters that influence the physics of the fluid flow: the dimensionless pressure gradient  $\Pi_{p,z}$ , the power-law exponent  $n$ , and the screw-pitch ratio  $t/D_b$ . Based on these parameters, we carried out a comprehensive numerical parametric study evaluating viscous dissipation and flow rate. Here, we present four heuristic models that predict the viscous dissipation of a power-law fluid in the melt-conveying zone of single-screw extruders. For one-dimensional and two-dimensional flows, we developed models for both a given pressure gradient and a given throughput. The approximation equations obtained allow fast and stable prediction without the need for numerical simulations of viscous dissipation. The accuracy of the heuristic models developed was validated in an error analysis, which showed that our approaches provide excellent approximations of the numerical results. POLYM. ENG. SCI., 58:2055–2070, 2018. © 2018 The Authors Polymer Engineering & Science published by Wiley Periodicals, Inc. on behalf of Society of Plastics Engineers**

## INTRODUCTION

Single-screw extruders are the most important equipment in polymer processing. In smooth-bore extruders, the melt-conveying zone controls the flow rate. It is usually analyzed using the flat-channel model, which was first introduced by Rowell and Finlayson [1, 2], who developed a one-dimensional isothermal Newtonian model studying the melt-conveying section of a single-screw extruder. Several further studies have investigated the melt-conveying behavior of isothermal Newtonian fluids and provide analytical solutions. Carley et al. [3] developed a Newtonian model with the flow rate as a linear superposition of drag and pressure flows, and additionally investigated tapered screw

channels. Mohr et al. [4] and Mohr and Mallouk [5] studied the transverse flow in a single-screw extruder, giving special consideration to the shear imposed on the fluid. They were the first to consider the pressure gradient in the transverse direction. In addition to throughput and the pressure distribution, Mohr and Mallouk [5] also calculated the power requirement.

The classical Newtonian pumping model gives first insights into the flow mechanisms and flow patterns of the melt-conveying zone in single-screw extruders. However, for a more accurate model the non-Newtonian behavior of polymer melts must be considered. For non-Newtonian fluids, the drag- and pressure flows cannot be analyzed independently, because they influence each other due to the shear-rate-dependent viscosity. Further, the transverse flow influences the flow in the down-channel direction, albeit not directly but via the shear-rate-dependent viscosity. Even for the simplest case—a one-dimensional isothermal flow of a power-law fluid—an exact analytical solution has not yet been found [6]. Rotem and Shinnar [7] derived numerical solutions for the one-dimensional flow of power-law fluids. Griffith [8] derived numerical results for both isothermal and nonisothermal two-dimensional flows of power-law fluids for a hydrodynamic and thermally fully developed flow in a single-screw extruder. In the nonisothermal calculation, constant fluid temperature is considered for one streamline. Zamodits and Pearson [9] followed a similar approach, using a comprehensive set of parameters. Booy [10] investigated the effect on the effective viscosity in power-law fluids in screw extruders and the channel efficiency by comparing the energy dissipated in the screw channel with the energy input for building up the discharge pressure for the given volumetric throughput for isothermal flow. A detailed presentation of the traditional pumping models was presented by Tadmor and Klein [11].

To avoid complex numerical calculations, approximation equations were introduced for the isothermal non-Newtonian pressure throughput behavior of the single-screw melt-conveying zone. Rauwendaal [6, 12] presented correction factors that depend on the power-law exponent  $n$  for the drag- and pressure flows. Using these correction factors allows the Newtonian output pressure calculation to be used. Rauwendaal's approximation is valid for helix angles in the range of  $15^\circ$ – $25^\circ$ . Potente [13] presented a non-linear approximation, but it is valid only in the range  $0.55$ – $0.6 \leq \Pi_V \leq 1$ , where  $\Pi_V$  is the dimensionless throughput. An improved approximation that divides the parameter range of the melt-conveying zone into eight regions with different values for the coefficients was given by White and Potente [14]. Pachner et al. [15] presented a generalized two-dimensional output model that is valid across the full application range of polymer melts and for both positive and negative dimensionless pressure gradients, that is, for both pressure build-up and overridden zones. Marschik et al. [16, 17] presented a three-dimensional output

Correspondence to: W. Roland; e-mail: wolfgang.roland@jku.at

Contract grant sponsor: Austrian federal government; Contract grant sponsor: The federal state of Upper Austria; Contract grant sponsor: Österreichische Forschungsförderungsgesellschaft  
DOI 10.1002/pen.24817

Published online in Wiley Online Library (wileyonlinelibrary.com).

© 2018 The Authors Polymer Engineering & Science published by Wiley Periodicals, Inc. on behalf of Society of Plastics Engineers

This is an open access article under the terms of the Creative Commons Attribution-NonCommercial-NoDerivs License, which permits use and distribution in any medium, provided the original work is properly cited, the use is non-commercial and no modifications or adaptations are made.

model for smooth-bore single screw-extruders as well as for smooth- and grooved-feed extruders, additionally taking into account the effect of the flight flanks on the flow rate. A heuristic approximation equation was developed for predicting the dimensionless throughput depending on the dimensionless pressure gradient, the power-law exponent, the screw-pitch ratio, and the channel-height to channel-width ratio. The novelty of the last sources cited [15–17] lies in the generation of an analytical relationship using symbolic regression based on genetic programming. Koza [18] was the first who investigated this method in detail in 1992. Genetic programming has also been applied successfully in other fields. Bramerdorfer et al. [19] performed FE simulations on permanent-magnet synchronous machines, using the simulation results to develop a dynamic motor model by means of symbolic regression employing genetic programming. This method is not limited to simulation data, but can also be applied to experimental data, where data preprocessing plays an important role. Lughofer et al. [20] applied symbolic regression using genetic programming to identify the key metrics of wet tribological systems using experimental data.

Aside from the isothermal throughput pressure behavior of the melt-conveying section, the development of the axial melt temperature plays an important role. Viscous dissipation is the main effect causing melt-temperature increases in the extrusion direction that effects the throughput behavior due to the temperature-dependent viscosity of polymer melts. Tadmor and Klein [11] showed a method for calculating the axial temperature distribution for adiabatic extrusion of Newtonian melts with temperature-dependent viscosity for a given volumetric throughput. Potente [13, 21] described the screw-drive power for a two-dimensional power-law fluid and showed how to perform a non-isothermal extruder calculation for a constant Brinkman number. However, the screw-drive power is not directly responsible for the temperature increase rather viscous dissipation causes the temperature increase. Campbell et al. [22] investigated viscous dissipation in Newtonian fluids, considering both a barrel and a screw rotation theory. Rauwendaal [6] presented various analytical models for the temperature increase in single-screw extruders. His work described the effect of temperature-dependent viscosity on the axial melt-temperature development in two cases: for an adiabatic condition and for a given heat flux through the extruder barrel. However, in these calculations the viscous dissipation is approximated by a simple drag flow of a power-law fluid, ignoring the additional viscous dissipation due to the superposed pressure flow. Derezinski [23–25] presented curves for the melt-temperature development based on numerical calculations considering heat transfer coefficients for the heat flux through the barrel wall, but a Newtonian temperature-dependent viscosity model is used to calculate the viscosity based on a representative shear rate. All of these models for calculating the axial melt-temperature profile are based on a lumped form of the energy equation that yields a bulk melt-temperature. Predicting the melt-temperature both in the channel direction and across the cross channel requires complex and time-consuming 3D simulations (e.g., CFD or finite element method, FEM) [6].

The viscous dissipation for a two-dimensional flow of a power-law fluid has been analyzed by means of numerical methods [26]. Here, we analyze the viscous dissipation in the melt-conveying zone of a single-screw extruder and propose generalized heuristic models for predicting the viscous dissipation of the

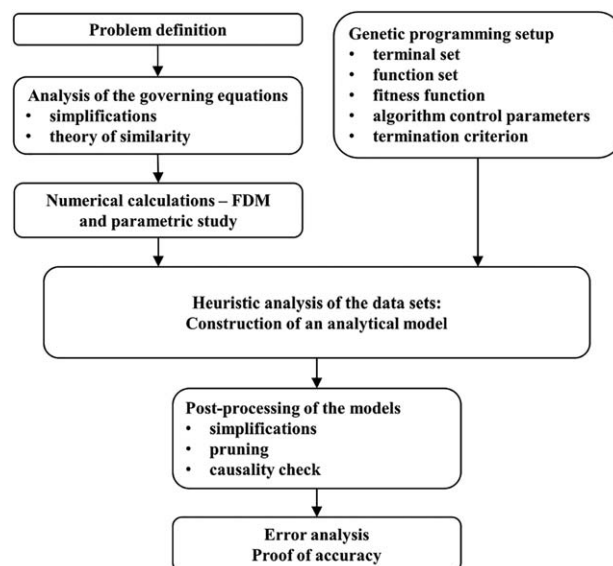


FIG. 1. Schematic work-flow diagram of the numerical and heuristic analyses of viscous dissipation.

polymer melt flow. These models can be used to calculate the axial melt-temperature profile and consequently the non-isothermal pressure throughput behavior. We derived the heuristic models by first simplifying the governing equations and transforming them into dimensionless form applying the theory of similarity. Two comprehensive parameter sets were created varying the independent dimensionless influencing parameters. The nonlinear governing equations obtained were then solved numerically by means of the finite difference method (FDM) yielding a comprehensive parametric study. Based on the numerical results, approximation equations were generated by means of symbolic regression using genetic programming. These models were then simplified, and finally an error analysis was conducted. A schematic of the work-flow is shown in Fig. 1.

## FUNDAMENTALS

Unwinding the helical screw channel, the melt-conveying section of a single-screw extruder can be considered as a flat, rectangular channel. Further, the kinematics are reversed—the screw is considered to be stationary and the barrel to be rotating about the screw. We thus obtain the well-known flat-channel model with the top plate moving at the velocity  $v_b$ . The flat-channel model is widely accepted and used for modeling flow in single-screw extrusion, but one must bear in mind that curvature influences the melt flow, especially for deep screw channels. The screw geometry and the corresponding flat-channel model are shown in Fig. 2. Flight effects and leakage flow over the flight gap  $\delta$  are ignored. For shallow screw channels with  $h/w < 0.1$  the effect of the screw flights on the polymer melt flow can be omitted [6]. The circumferential velocity  $v_b$  is calculated according to Eq. 1 with the barrel diameter  $D_b$  and the screw speed  $N$ . Depending on screw pitch  $t$ , the circumferential speed is divided into a down-channel velocity  $v_{b,z}$  (Eq. 2) and a cross-channel velocity  $v_{b,x}$  (Eq. 3) component.

$$v_b = D_b \pi N; \quad (1)$$

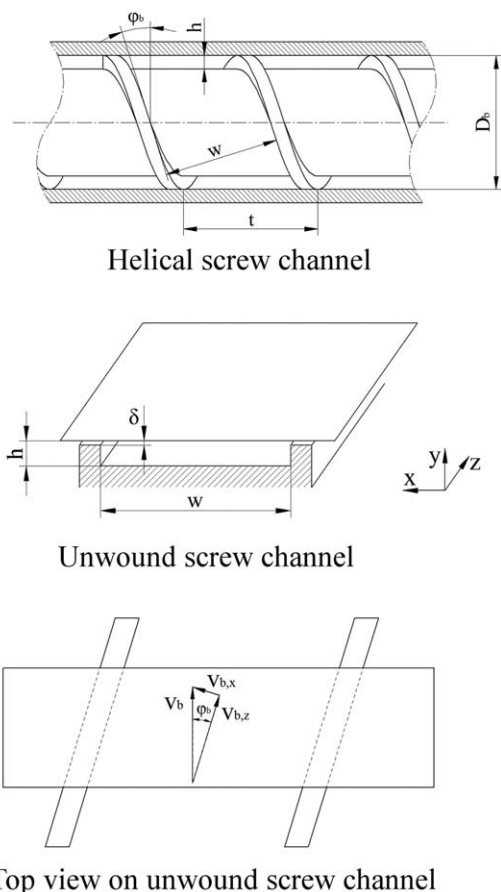


FIG. 2. Wound and unwound screw channel of a single-screw extruder. Helical screw channel (top), unwound screw channel (middle), and top-view of the unwound screw channel and the velocity components of the top plate (bottom).

$$v_{b,z} = v_b \cos(\varphi_b); \quad (2)$$

$$v_{b,x} = v_b \sin(\varphi_b) \quad (3)$$

with

$$\varphi_b = \arctan\left(\frac{t}{D_b \pi}\right). \quad (4)$$

Polymer melts are highly non-Newtonian and exhibit shear-thinning behavior. This means that the viscosity  $\eta$  decreases with increasing shear rate  $\dot{\gamma}$ . This pseudo-plastic fluid behavior of polymer melts is considered by the power-law model (Eq. 5), with the consistency  $K$  and the power-law exponent  $n$ , where  $n < 1$  for polymer melts [27].

$$\eta = K |\dot{\gamma}|^{n-1}. \quad (5)$$

In addition to the simplifications mentioned above-ignoring the curvature effect, flight effects, and leakage flow-we assume an isothermal, stationary, incompressible, and fully developed flow.

#### Governing Equations

Determining viscous dissipation requires the velocity field to be calculated first by solving the equation of continuity (Eq. 6) and the equation of motion (Eq. 7). With the resulting velocity distribution, the viscous dissipation can be evaluated by the

energy equation. In Cartesian coordinates, the Equations of continuity and motion are given respectively by

$$\frac{\partial \rho}{\partial t} + \frac{\partial}{\partial x}(\rho v_x) + \frac{\partial}{\partial y}(\rho v_y) + \frac{\partial}{\partial z}(\rho v_z) = 0 \quad (6)$$

$$\begin{aligned} \frac{\partial(\rho v_x)}{\partial t} + \frac{\partial(\rho v_x v_x)}{\partial x} + \frac{\partial(\rho v_y v_x)}{\partial y} + \frac{\partial(\rho v_z v_x)}{\partial z} = \\ -\frac{\partial p}{\partial x} + \left(\frac{\partial \tau_{xx}}{\partial x} + \frac{\partial \tau_{yx}}{\partial y} + \frac{\partial \tau_{zx}}{\partial z}\right) + \rho g_x \end{aligned} \quad (7)$$

$$\begin{aligned} \frac{\partial(\rho v_y)}{\partial t} + \frac{\partial(\rho v_x v_y)}{\partial x} + \frac{\partial(\rho v_y v_y)}{\partial y} + \frac{\partial(\rho v_z v_y)}{\partial z} = \\ -\frac{\partial p}{\partial y} + \left(\frac{\partial \tau_{xy}}{\partial x} + \frac{\partial \tau_{yy}}{\partial y} + \frac{\partial \tau_{zy}}{\partial z}\right) + \rho g_y \end{aligned}$$

$$\begin{aligned} \frac{\partial(\rho v_z)}{\partial t} + \frac{\partial(\rho v_x v_z)}{\partial x} + \frac{\partial(\rho v_y v_z)}{\partial y} + \frac{\partial(\rho v_z v_z)}{\partial z} = \\ -\frac{\partial p}{\partial z} + \left(\frac{\partial \tau_{xz}}{\partial x} + \frac{\partial \tau_{yz}}{\partial y} + \frac{\partial \tau_{zz}}{\partial z}\right) + \rho g_z \end{aligned}$$

where  $\tau_{ij}$  is the corresponding component of the stress tensor  $\tau$ , which is calculated based on the viscosity  $\eta$  and the rate-of-deformation tensor  $D$  by Eq. 8. The rate-of-deformation tensor  $D$  is defined by Eq. 9 with the velocity vector  $\mathbf{v} = (v_x, v_y, v_z)^T$  [27].

$$\tau = 2 \eta D. \quad (8)$$

$$D = \frac{1}{2} \left( \nabla \mathbf{v} + (\nabla \mathbf{v})^T \right). \quad (9)$$

In Cartesian coordinates, we obtain for the rate-of-deformation tensor:

$$D = \frac{1}{2} \begin{pmatrix} 2 \frac{\partial v_x}{\partial x} & \frac{\partial v_y}{\partial x} + \frac{\partial v_x}{\partial y} & \frac{\partial v_z}{\partial x} + \frac{\partial v_x}{\partial z} \\ \frac{\partial v_x}{\partial y} + \frac{\partial v_y}{\partial x} & 2 \frac{\partial v_y}{\partial y} & \frac{\partial v_z}{\partial y} + \frac{\partial v_y}{\partial z} \\ \frac{\partial v_x}{\partial z} + \frac{\partial v_z}{\partial x} & \frac{\partial v_y}{\partial z} + \frac{\partial v_z}{\partial y} & 2 \frac{\partial v_z}{\partial z} \end{pmatrix}. \quad (10)$$

The magnitude of the shear rate, which is a scalar quantity and important for determining the non-Newtonian viscosity, is related to the second invariant of the rate-of-deformation tensor as follows:

$$|\dot{\gamma}| = \sqrt{2 (D : D)}, \quad (11)$$

$$|\dot{\gamma}| = \left\{ 2 \left[ \left( \frac{\partial v_x}{\partial x} \right)^2 + \left( \frac{\partial v_y}{\partial y} \right)^2 + \left( \frac{\partial v_z}{\partial z} \right)^2 \right] + \left( \frac{\partial v_x}{\partial y} + \frac{\partial v_y}{\partial x} \right)^2 + \left( \frac{\partial v_x}{\partial z} + \frac{\partial v_z}{\partial x} \right)^2 + \left( \frac{\partial v_y}{\partial z} + \frac{\partial v_z}{\partial y} \right)^2 \right\}^{\frac{1}{2}} \quad (12)$$

In this work, the influence of the flights is ignored, which means that a two-dimensional velocity profile is considered. Additionally, the following assumptions are made: (i) the flow is stationary and thus independent of time; (ii) the fluid is incompressible; (iii) gravitation is ignored; and (iv) the flow is fully developed. Based on these assumptions, the velocity vector is reduced to Eq. 13 with down-channel velocity and cross-channel velocity being functions of the channel-height coordinate  $y$  only.

$$\mathbf{v} = \begin{pmatrix} v_x(y) \\ 0 \\ v_z(y) \end{pmatrix}. \quad (13)$$

Further, the equation of continuity and the equation of motion are reduced due to the flow assumptions. In the equation of continuity (Eq. 6) all terms become zero, which means it need not be taken into account in the further analysis. Applying the relation between viscous stresses and rate-of-deformation (Eq. 8) reduces the equation of motion to Eq. 14 for the  $x$ -direction and to Eq. 15 for the  $z$ -direction. Considering the flow assumptions cancels out all inertia terms. However, since for polymer melts the viscous forces are considerably higher than the gravitational and inertial forces, the latter two can be ignored in any case. The ratio of inertial to viscous forces is described by the Reynolds number  $Re$ . For a typical polymer melt flow with  $\eta=500$  Pas,  $h=10$  mm,  $v=0.2$  m/s, and  $\rho=800$  kg/m<sup>3</sup>, the Reynolds number is  $Re=3.2 \cdot 10^{-3}$ . For  $Re \ll 1$ , the inertia terms can be neglected and the flow equations are reduced to Stokes flow. The magnitude of the shear rate  $|\dot{\gamma}|$  is reduced to Eq. 16. Applying the power-law model (Eq. 5) allows the viscosity to be calculated according to Eq. 17 being a function of the channel-height coordinate  $y$ .

$$\frac{\partial p}{\partial x} = \frac{\partial}{\partial y} \left( \eta(y) \frac{\partial v_x}{\partial y} \right). \quad (14)$$

$$\frac{\partial p}{\partial z} = \frac{\partial}{\partial y} \left( \eta(y) \frac{\partial v_z}{\partial y} \right). \quad (15)$$

$$|\dot{\gamma}| = \left\{ \left( \frac{\partial v_x}{\partial y} \right)^2 + \left( \frac{\partial v_z}{\partial y} \right)^2 \right\}^{\frac{1}{2}}. \quad (16)$$

$$\eta = K \left\{ \left( \frac{\partial v_x}{\partial y} \right)^2 + \left( \frac{\partial v_z}{\partial y} \right)^2 \right\}^{\frac{n-1}{2}}. \quad (17)$$

Solving the down-channel and cross-channel velocity profiles  $v_z(y)$  and  $v_x(y)$  requires boundary conditions. A wall-adhering fluid is assumed, which is also known as the no-slip condition. With the boundary conditions (Eqs. 18–21), the velocity profiles can be determined for a given down-channel pressure gradient  $dp/dz$ . Additionally, we must consider that the volumetric cross-channel flow has to be zero (Eq. 22), which determines the cross-channel pressure gradient. The volumetric flow rate  $\dot{V}$  of the melt-conveying section is calculated by integrating the down-channel velocity profile over the cross-channel area (Eq. 23), with  $i$  as the number of parallel screw channels:

$$v_x(y=0)=0, \quad (18)$$

$$v_x(y=h)=v_{b,x}, \quad (19)$$

$$v_z(y=0)=0, \quad (20)$$

$$v_z(y=h)=v_{b,z}, \quad (21)$$

$$\dot{V}_x = \int_0^h v_x(y) dy = 0, \quad (22)$$

$$\dot{V} = i \int_0^h v_z(y) dy. \quad (23)$$

The viscous dissipation per unit volume can be derived from the energy equation and is defined by Eq. 24. With the simplifications

made above and applying Eq. 8 for the viscous stresses, the viscous dissipation per unit volume is reduced to Eq. 25. The total viscous dissipation  $\dot{Q}_{\text{diss}}$  over the channel is the integral of the specific dissipation over the cross-channel area (Eq. 26):

$$\dot{q}_{\text{diss}} = \left( \tau_{xx} \frac{\partial v_x}{\partial x} + \tau_{yy} \frac{\partial v_y}{\partial y} + \tau_{zz} \frac{\partial v_z}{\partial z} \right) + \left[ \tau_{xy} \left( \frac{\partial v_x}{\partial y} + \frac{\partial v_y}{\partial x} \right) + \tau_{xz} \left( \frac{\partial v_x}{\partial z} + \frac{\partial v_z}{\partial x} \right) + \tau_{yz} \left( \frac{\partial v_y}{\partial z} + \frac{\partial v_z}{\partial y} \right) \right], \quad (24)$$

$$\dot{q}_{\text{diss}} = \eta \left[ \left( \frac{\partial v_x}{\partial y} \right)^2 + \left( \frac{\partial v_z}{\partial y} \right)^2 \right], \quad (25)$$

$$\dot{Q}_{\text{Diss}} = i \int_0^h \dot{q}_{\text{diss}}(y) dy = i \int_0^h \eta \left[ \left( \frac{\partial v_x}{\partial y} \right)^2 + \left( \frac{\partial v_z}{\partial y} \right)^2 \right] dy. \quad (26)$$

### Theory of Similarity

The equations of motion with the corresponding boundary conditions presented above are non-linear partial differential equations and can be solved numerically. However, first the governing equations are transformed into dimensionless form by applying the theory of similarity and dimensional analysis. Generally, two systems that have the same dimensionless values are similar and exhibit the same physical behavior. In our case, this means that two melt-conveying sections with identical dimensionless values are similar in terms of their underlying physics (e.g., velocity distribution, viscosity distribution), but are scaled to different ranges. Hence, the solution for a specific set of dimensionless input parameters is applicable to all dimensional variations resulting in this specific set of dimensionless parameters. Due to scaling, the number of parameters can be reduced, and the results obtained are more widely applicable [28]. To translate the governing equations into a dimensionless space, we introduce the dimensionless coordinate  $\xi$  (Eq. 27), the dimensionless cross-channel velocity  $v_x$  (Eq. 28), and the dimensionless down-channel velocity  $v_z$  (Eq. 29).

$$\xi = \frac{y}{h}. \quad (27)$$

$$v_x = \frac{v_x}{v_{b,x}} = \frac{1}{\tan(\varphi_b)} \frac{v_x}{v_{b,z}}. \quad (28)$$

$$v_z = \frac{v_z}{v_{b,z}}. \quad (29)$$

Using these definitions (Eqs. 27–29) we can re-write the magnitude of the shear rate in dimensionless form (Eq. 30). Further, for convenience we define a dimensionless viscosity (Eq. 31):

$$|\dot{\gamma}^*| = \frac{h}{v_{b,z}} |\dot{\gamma}| = \left[ \left( \frac{\partial v_z}{\partial \xi} \right)^2 + \tan^2(\varphi_b) \left( \frac{\partial v_x}{\partial \xi} \right)^2 \right]^{\frac{1}{2}}, \quad (30)$$

$$\eta^* = \frac{\eta}{K} \frac{h^{n-1}}{v_{b,z}^{n-1}} = |\dot{\gamma}^*|^{n-1} = \left[ \left( \frac{\partial v_z}{\partial \xi} \right)^2 + \tan^2(\varphi_b) \left( \frac{\partial v_x}{\partial \xi} \right)^2 \right]^{\frac{n-1}{2}}. \quad (31)$$

Applying the dimensionless variables, we can transform the momentum equations into dimensionless form (Eqs. 32 and 33) with the dimensionless down-channel pressure gradient  $\Pi_{p,z}$



(Eq. 34) and the dimensionless cross-channel pressure gradient  $\Pi_{p,x}$  (Eq. 35):

$$6 \cdot \Pi_{p,z} = \frac{\partial}{\partial \xi} \left( \eta^* \frac{\partial v_z}{\partial \xi} \right), \quad (32)$$

$$6 \cdot \Pi_{p,x} = \tan(\varphi_b) \frac{\partial}{\partial \xi} \left( \eta^* \frac{\partial v_x}{\partial \xi} \right), \quad (33)$$

$$\Pi_{p,z} = \frac{\frac{\partial p}{\partial z} h^{n+1}}{6 K v_{b,z}^n}, \quad (34)$$

$$\Pi_{p,x} = \frac{\frac{\partial p}{\partial x} h^{n+1}}{6 K v_{b,z}^n}. \quad (35)$$

Furthermore, for solving the dimensionless equations of motion, the boundary conditions and the side condition are re-written in dimensionless form:

$$v_x(\xi=0)=0, \quad (36)$$

$$v_x(\xi=1)=1, \quad (37)$$

$$v_z(\xi=0)=0, \quad (38)$$

$$v_z(\xi=1)=1, \quad (39)$$

$$\int_0^1 v_x(\xi) d\xi = 0. \quad (40)$$

This coupled system of nonlinear partial differential equations has three independent influencing parameters: (i) the dimensionless down-channel pressure gradient  $\Pi_{p,z}$ , (ii) the screw-pitch ratio  $t/D_b$  represented by  $\tan(\varphi_b)$ , and (iii) the power-law exponent  $n$  in the dimensionless viscosity  $\eta^*$ . Depending on the size of the pitch angle, two limits can be identified. If  $\varphi_b=0^\circ$  and thus,  $\tan(\varphi_b)=0$ , the cross-channel velocity components in the governing equations vanish. The system is reduced to a one-dimensional flow, a simple Poiseuille-Couette flow of a power-law fluid between two parallel plates. Thus, only the equation of motion (Eq. 32) in the down-channel direction remains, and the dimensionless shear rate and dimensionless viscosity are reduced to Eqs. 41 and 42, respectively. Physically, this means that there is no cross-channel flow in the screw channel. The second limit is for  $\varphi_b=90^\circ$  and thus,  $\tan(\varphi_b)=\infty$ , where the cross-channel flow becomes dominant and the down-channel velocity component can be ignored.

$$|\dot{\gamma}^*| = \left( \frac{\partial v_z}{\partial \xi} \right). \quad (41)$$

$$\eta^* = \left( \frac{\partial v_z}{\partial \xi} \right)^{n-1}. \quad (42)$$

Comparing the dimensional and dimensionless systems, we see that by applying the theory of similarity the number of influencing parameters has been reduced from seven in the dimensional representation ( $D_b$ ,  $t$ ,  $h$ ,  $N$ ,  $K$ ,  $n$ , and  $dp/dz$ ) to three in the dimensionless representation ( $\Pi_{p,z}$ ,  $n$ , and  $t/D_b$ ).

Based on the dimensionless down-channel velocity profile  $v_z(\xi)$ , the dimensionless volume throughput  $\Pi_V$  (Eq. 43) can be evaluated according to Eq. 44. Further, the specific dissipation can be re-written in dimensionless form, which results in the dimensionless specific dissipation  $\pi_q$  (Eq. 45). Analogously to

TABLE 1. Ranges of variation for  $t/D_b$  and  $n$  in the two-dimensional analysis.

Quantity	Min	Max	Increment
$t/D_b$	0.5	2.0	0.1
$n$	0.2	1.0	0.1

the dimensionless throughput, the dimensionless dissipation  $\Pi_Q$  (Eq. 46) is calculated based on the dimensionless specific dissipation  $\pi_q(\xi)$  according to Eq. 47.

$$\Pi_V = \frac{2 \dot{V}}{i w h v_{b,z}}. \quad (43)$$

$$\Pi_V = \int_0^1 v_z(\xi) d\xi. \quad (44)$$

$$\pi_q(\xi) = \frac{\dot{q}_{\text{diss}} h^{n+1}}{K v_{b,z}^{n+1}} = \eta^* \left[ \left( \frac{\partial v_z}{\partial \xi} \right)^2 + \tan^2(\varphi_b) \left( \frac{\partial v_x}{\partial \xi} \right)^2 \right]. \quad (45)$$

$$\Pi_Q = \frac{\dot{Q}_{\text{Diss}} h^n}{i w K v_{b,z}^{n+1}}. \quad (46)$$

$$\Pi_Q = \int_0^1 \pi_q(\xi) d\xi = \int_0^1 \left[ \left( \frac{\partial v_z}{\partial \xi} \right)^2 + \tan^2(\varphi_b) \left( \frac{\partial v_x}{\partial \xi} \right)^2 \right]^{\frac{n+1}{2}} d\xi. \quad (47)$$

Again, taking the limit for the pitch angle with  $\varphi_b=0^\circ$  into account, which represents a one-dimensional flow, the dimensionless specific dissipation is reduced to Eq. 48, and the dimensionless dissipation to Eq. 49.

$$\pi_q(\xi) = \left( \frac{\partial v_z}{\partial \xi} \right)^{n+1}. \quad (48)$$

$$\Pi_Q = \int_0^1 \left( \frac{\partial v_z}{\partial \xi} \right)^{n+1} d\xi. \quad (49)$$

Taking the findings of the dimensional analysis into account, we created two sets of independent design points by varying the dimensionless influencing parameters  $\Pi_{p,z}$ ,  $t/D_b$ , and  $n$ . The first set is for the one-dimensional case with  $t/D_b=0$ , and the second for the two-dimensional case. For the one-dimensional and two-dimensional analyses, respectively, total numbers of 729 and 8,784 independent design points were created. In both analyses, the power-law exponent was varied within the range from  $n=0.2$  to  $n=1.0$  by increments of  $\Delta n=0.1$ . This range applies to almost all polymer melts in industrial polymer extrusion. For the one-dimensional analysis the screw-pitch ratio was  $t/D_b=0$ , and for the two-dimensional analysis it was varied within the range from  $t/D_b=0.5$  to  $t/D_b=2.0$  with an increment of  $\Delta t/D_b=0.1$ . The range of the dimensionless down-channel pressure gradient was based on the screw-pitch ratio and the power-law exponent. The minimum and maximum dimensionless down-channel pressure gradients  $\Pi_{p,z}$  were chosen such that a maximum dimensionless throughput of  $\Pi_{V,\text{max}} \geq 2.0$  and a minimum dimensionless throughput of  $\Pi_{V,\text{min}} \leq 0.0$  were approximately achieved. This resulted in a different range of  $\Pi_{p,z}$  for each set of  $t/D_b$  and  $n$ . For the one-dimensional and two-dimensional analyses the range of  $\Pi_{p,z}$  was divided into 80 and 60 equidistant divisions, respectively. Table 1 summarizes

TABLE 2. Ranges of variation for  $\Pi_{p,z}$  depending on the power-law exponent in the one-dimensional analysis.

$n$	Min	Max	Increment
1.0	-1.0	1.0	0.0250
0.9	-1.0	1.0	0.0250
0.8	-0.925	0.925	0.0231
0.7	-0.8325	0.8325	0.0208
0.6	-0.7701	0.7701	0.0193
0.5	-0.6931	0.6931	0.0173
0.4	-0.6238	0.6238	0.0156
0.3	-0.5614	0.5614	0.0140
0.2	-0.5052	0.5052	0.0126

the variations of  $t/D_b$  and  $n$  for the two-dimensional analysis, while Table 2 shows the variation of  $\Pi_{p,z}$  depending on the power-law exponent for the one-dimensional analysis. In the two-dimensional analysis, the range of  $\Pi_{p,z}$  was similar, but differs slightly for each value of  $t/D_b$ .

## NUMERICAL CALCULATIONS

Applying the theory of similarity reduced the number of influencing parameters significantly resulting to the following three: (i)  $\Pi_{p,z}$ , (ii)  $t/D_b$ , and (iii)  $n$ . Solving the nonlinear, coupled dimensionless equations of motion requires numerical methods. As a result, we obtain the dimensionless down-channel and dimensionless cross-channel velocities, which are needed to evaluate the main target values—the dimensionless volume throughput  $\Pi_V$  and the dimensionless dissipation  $\Pi_Q$ . For this purpose, various numerical techniques are available, for instance the shooting method, the FDM, and the FEM. It has been shown that all three methods are suitable for solving the dimensionless governing equations 26. We chose the FDM to calculate the numerical solutions.

### Numerical Solution

The basic idea of FDM is to approximate the derivatives by difference quotients, thus transforming the differential into algebraic equations. Additionally, the equations are linearized, which leads to a system of linear equations that can easily be solved. The nonlinear behavior is addressed by iteratively solving a linearized system. We used the second-order difference quotient (Eq. 50) with the discretization interval  $\Delta x$ . For each inner node, this difference quotient is applied first to the outer and then to the inner derivative of the dimensionless momentum equations (Eqs. 32 and 33), with the discretization interval  $\Delta \xi$ . Hence, the dimensionless equations of motion can be approximated, respectively, by Eqs. 51 and 52 for the down-channel and cross-channel directions for each inner node. For the boundary nodes, this approximation is not needed, because these values are given by the boundary conditions. For the dimensionless viscosity between two nodes, the average is simply considered (Eq. 53). The iterative processing of the non-linear and coupled behavior is then performed, starting with initial Newtonian viscosity  $\eta^* = 1$  in the first run. For subsequent iterations, the viscosity is determined based on the velocity profile derived from the previous iterations. Consequently, the down- and cross-channel velocities can be solved independently in each iteration.

Processing continues until physical convergence is reached. This means that the dimensionless volume flow rate and the dimensionless dissipation have converged.

$$\left(\frac{\partial f}{\partial x}\right)_{i+1/2} = \frac{f_{i+1} - f_i}{\Delta x}. \quad (50)$$

$$6 \Pi_{p,z} \Delta \xi^2 = v_{z,i-1} \eta_{i-1/2}^* - v_{z,i} \left( \eta_{i+1/2}^* + \eta_{i-1/2}^* \right) + v_{z,i+1} \eta_{i+1/2}^*. \quad (51)$$

$$\frac{6 \Pi_{p,x} \Delta \xi^2}{\tan(\varphi_b)} = v_{x,i-1} \eta_{i-1/2}^* - v_{x,i} \left( \eta_{i+1/2}^* + \eta_{i-1/2}^* \right) + v_{x,i+1} \eta_{i+1/2}^*. \quad (52)$$

$$\eta_{i+1/2}^* = \frac{1}{2} (\eta_i^* + \eta_{i+1}^*). \quad (53)$$

Assembling the equations for each node in both the down- and cross-channel directions allows them to be arranged in matrix form, which yields a system of linear equations for the down- and cross-channel velocity components—Eqs. 54 and 55, respectively. In the system of equations for the cross-channel direction, the additional condition that the cross-channel flow be zero (Eq. 40) is included. The integration is done numerically applying the Simpson rule. If  $N$  is the number of equidistant divisions, matrix  $A_z$  is of size  $(N-1) \times (N-1)$  and  $A_x$  is of size  $N \times N$ . The number of nodes is  $N+1$ . For details of how the linear equation systems are built, see the Appendix.

$$A_z \cdot v_z = p_z. \quad (54)$$

$$A_x \cdot v_x = p_x. \quad (55)$$

With minor modifications, this method is also suitable for solving the one-dimensional case. To this end, the linear equation system in cross-channel direction and the cross-channel velocity component in the dimensionless viscosity are omitted. In this study, we divided the dimensionless channel height into 400 equidistant divisions, to obtain a total of 401 nodes. As abortion criterion, the dimensionless volume flow rate was chosen. The numerical iterations were stopped, when the change in the dimensionless volume flow rate was  $\Delta \Pi_V < 10^{-6}$  between two iterations. Both the number of nodes and the abortion criterion were tested for suitable for reaching a converged, mesh independent solution.

To ensure accurate results, we validated the numerical calculations with the analytical solution for the velocity profiles and the specific dissipation profile for the Newtonian case ( $n=1$ ). The dimensionless cross- and down-channel velocity profiles are given by Eqs. 56 and 57, respectively. Based on the dimensionless velocity profiles, the dimensionless specific dissipation is given by Eq. 58.

$$v_x(\xi) = 3 \xi^2 - 2 \xi. \quad (56)$$

$$v_z(\xi) = \xi + 3 \Pi_{p,z} (\xi^2 - \xi). \quad (57)$$

$$\pi_{q, \text{spez}} = [1 + 3 \Pi_{p,z} (2 \xi - 1)]^2 + \tan(\varphi_b)^2 [6 \xi - 2]^2. \quad (58)$$

Figure 3 shows the analytical and numerical velocity profiles for a Newtonian fluid with  $t/D_b = 1.0$  for three dimensionless pressure gradients, and Fig. 4 presents the analytical and numerical dimensionless specific dissipations. It can be seen that the

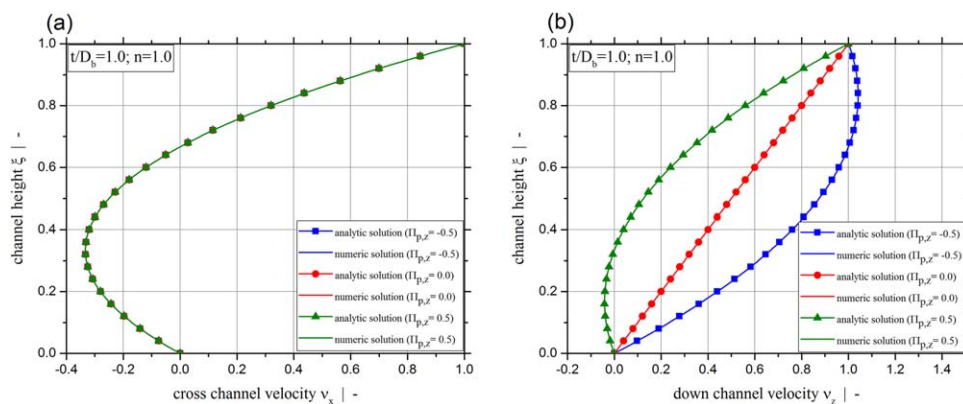


FIG. 3. Comparison of the analytical and numerical solutions for the cross-channel velocity profile (a) and the down-channel velocity profile (b) for  $t/D_b=1.0$  and three dimensionless pressure gradients ( $\Pi_{p,z}=-0.5$ ,  $\Pi_{p,z}=0.0$ ,  $\Pi_{p,z}=0.5$ ). [Color figure can be viewed at wileyonlinelibrary.com]

numerical and analytical solutions coincide for the Newtonian flow case.

#### Results of the Numerical Calculations

The comprehensive parametric study, containing, respectively, 729 and 8,784 independent design points for the one-dimensional and two-dimensional analyses, provides numerical solutions for the dimensionless volume flow rate  $\Pi_V$  and the dimensionless dissipation  $\Pi_Q$  as functions of the independent input parameters  $n$ ,  $t/D_b$ , and  $\Pi_{p,z}$ . These three parameters completely describe the flow under consideration in a single screw extruder. In addition to these two output parameters, the numerical calculation also gives results for the dimensionless cross-channel pressure gradient  $\Pi_{p,x}$  for each independent design point. In Fig. 5, the dimensionless volume flow rate  $\Pi_V$  of the one-dimensional analysis is shown as a function of the dimensionless down-channel pressure gradient  $\Pi_{p,z}$  for various power-law exponents  $n$ . The results are in very good agreement with

those of a one-dimensional analysis published by Rauwendaal [6]. For a Newtonian fluid, the throughput-pressure relationship shows the well-known linear behavior. With increasing non-Newtonian behavior (i.e., with decreasing power-law exponent) the throughput-pressure relationship becomes increasingly non-linear. Considering a constant dimensionless pressure gradient, the dimensionless throughput decreases with decreasing power-law exponent for positive dimensionless pressure gradients, whereas it increases for negative dimensionless pressure gradients. Figure 6 shows the dimensionless dissipation  $\Pi_Q$  of the one-dimensional analysis for various power-law exponents  $n$ . The relationship between dimensionless throughput and dimensionless down-channel pressure gradient means, that the dissipation can be plotted over both (Fig. 6a and b). It can be seen that minimum dimensionless dissipation occurs for pure drag flow ( $\Pi_{p,z}=0$  and  $\Pi_V=1$ ). With increasing positive or negative dimensionless pressure gradient (i.e., with decreasing or increasing dimensionless volume flow rate, respectively), dimensionless

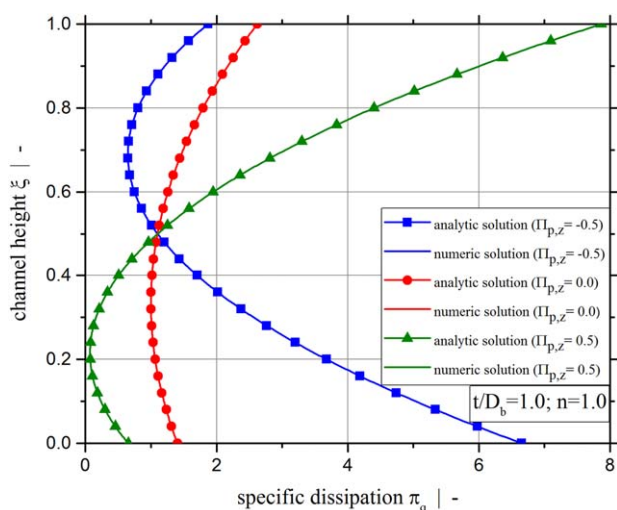


FIG. 4. Comparison of the analytical and numerical solutions for the dimensionless specific dissipation for  $t/D_b=1.0$  and three dimensionless pressure gradients ( $\Pi_{p,z}=-0.5$ ,  $\Pi_{p,z}=0.0$ , and  $\Pi_{p,z}=0.5$ ). [Color figure can be viewed at wileyonlinelibrary.com]

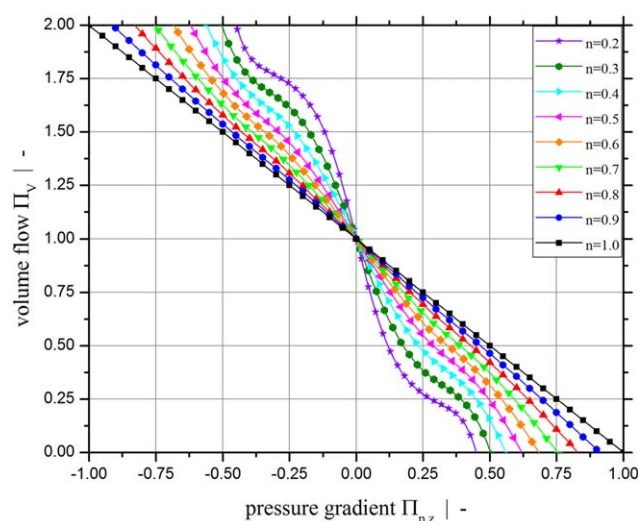


FIG. 5. Dimensionless volume flow  $\Pi_V$  of the one-dimensional analysis as a function of the dimensionless down-channel pressure gradient  $\Pi_{p,z}$  for various power-law exponents  $n$ . [Color figure can be viewed at wileyonlinelibrary.com]

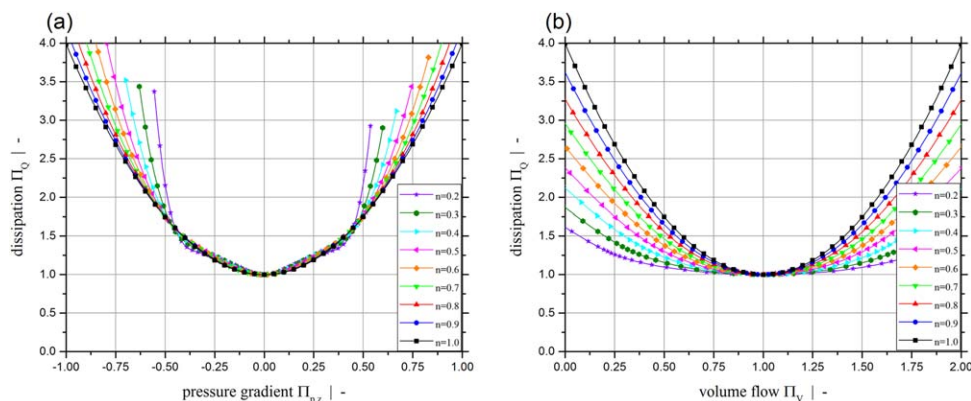


FIG. 6. Dimensionless dissipation  $\Pi_Q$  of the one-dimensional analysis as a function of the dimensionless down-channel pressure gradient  $\Pi_{p,z}$  (a) and as a function of the dimensionless volume flow rate  $\Pi_V$  (b) for various power-law exponents  $n$ . [Color figure can be viewed at wileyonlinelibrary.com]

dissipation increases. For moderate dimensionless pressure gradients, dimensionless dissipation is largely independent of the power-law exponent. At higher magnitudes of the dimensionless down-channel pressure gradient, it increases with decreasing power-law exponent for constant dimensionless pressure gradients. Considering a constant dimensionless volume flow rate, dimensionless dissipation decreases with decreasing power-law exponent.

Figures 5 and 6 show the results for dimensionless throughput and dimensionless dissipation from a one-dimensional analysis. However, note that more precise predictions of flow rate and viscous dissipation in single-screw extrusion requires, a two-dimensional analysis, that takes the influence of the screw-pitch ratio  $t/D_b$  into account. Figure 7 shows the dimensionless volume flow rate  $\Pi_V$  for a screw-pitch ratio of  $t/D_b = 1.0$  as a function of the dimensionless down-channel pressure gradient  $\Pi_{p,z}$  for various power-law exponents  $n$ . Generally, the two-dimensional analysis describes a behavior of the throughput pressure relation similar to that of the one-dimensional analysis.

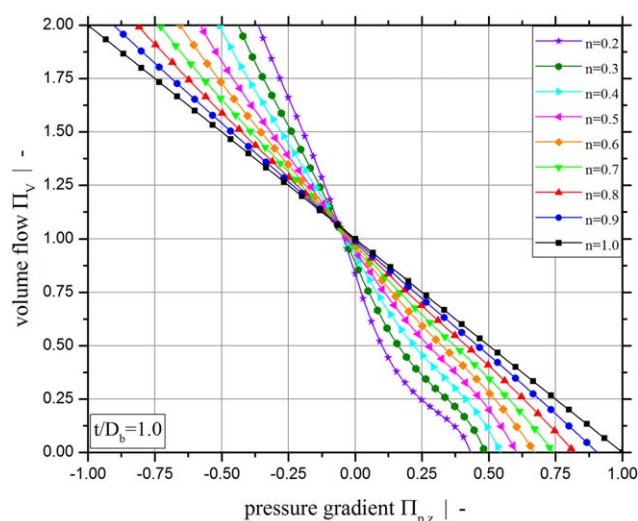


FIG. 7. Dimensionless volume flow  $\Pi_V$  of the two-dimensional analysis with a screw-pitch ratio  $t/D_b = 1.0$  as a function of the dimensionless down-channel pressure gradient  $\Pi_{p,z}$  for various power-law exponents  $n$ . [Color figure can be viewed at wileyonlinelibrary.com]

However, the lines are shifted due to the screw-pitch ratio  $t/D_b$ , which is shown in Fig. 8 for a power-law exponent of  $n = 0.5$ . For a Newtonian fluid, the one-dimensional and two-dimensional analyses deliver the same throughput-pressure relationship, but with decreasing power-law exponent, the difference becomes significant. In Fig. 8, it can be seen that the dimensionless volume flow rate decreases with increasing screw-pitch ratio for a constant dimensionless pressure gradient. Only for higher negative dimensionless pressure gradients does the flow rate increase. This can be explained by an increased shear rate that results in lower viscosity. Thus, in pressure build-up zones (positive dimensionless pressure gradient), the back pressure has a greater influence on the throughput. The two-dimensional results of the dimensionless volume flow rate agree very well with those presented in previous studies [6, 8, 10].

The screw-pitch ratio not only influences the throughput pressure relation, but also the dissipation. Its influence on the dimensionless dissipation is in fact more significant. Figure 9 shows the dimensionless dissipation  $\Pi_Q$  for a screw-pitch ratio

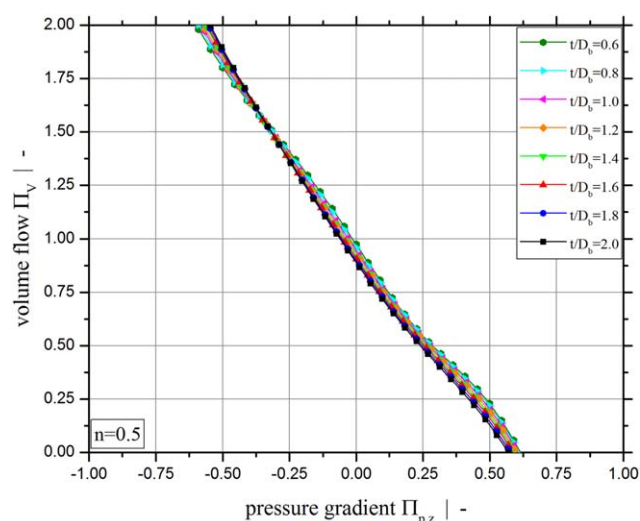


FIG. 8. Dimensionless volume flow  $\Pi_V$  of the two-dimensional analysis for a power-law exponent  $n = 0.5$  as a function of the dimensionless down-channel pressure gradient  $\Pi_{p,z}$  for various screw-pitch ratios  $t/D_b$ . [Color figure can be viewed at wileyonlinelibrary.com]



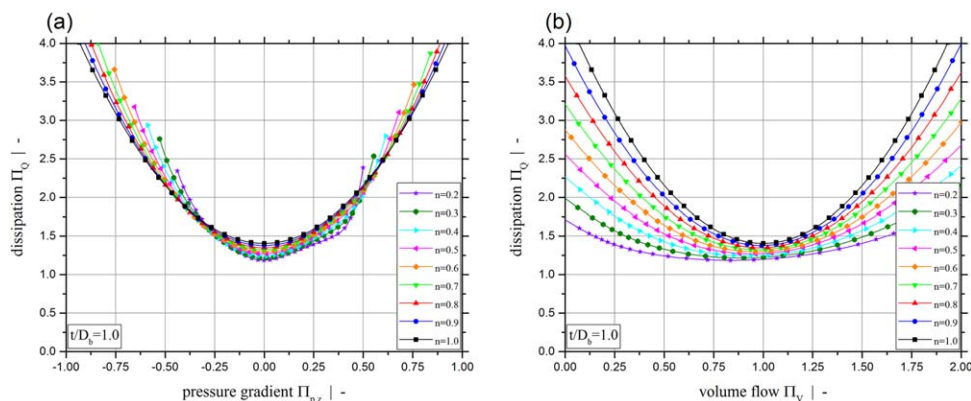


FIG. 9. Dimensionless dissipation  $\Pi_Q$  of the two-dimensional analysis with a screw-pitch ratio  $t/D_b = 1.0$  as a function of the dimensionless down-channel pressure gradient  $\Pi_{p,z}$  (a) and as a function of the dimensionless volume flow rate  $\Pi_V$  (b) for various power-law exponents  $n$ . [Color figure can be viewed at [wileyonlinelibrary.com](https://onlinelibrary.wiley.com)]

of  $t/D_b = 1.0$  as a function of the dimensionless down-channel pressure gradient  $\Pi_{p,z}$  (Fig. 9a) and as a function of the dimensionless volume flow rate  $\Pi_V$  (Fig. 9b) for different power-law exponents  $n$ . The relationships between dissipation and pressure gradient and between dissipation and throughput remain similar even if the cross-channel flow is considered. Nevertheless, in contrast to the one-dimensional approach, for moderate dimensionless pressure gradients dimensionless dissipation decreases with decreasing power-law exponent. Minimum dimensionless

dissipation still occurs for pure drag flow ( $\Pi_{p,z} = 0$ ), and dissipation increases with increasing positive and negative dimensionless pressure gradients. This result is in agreement with the specific dissipation profile  $\pi_q(\xi)$  shown in Fig. 10d for a power-law exponent  $n = 0.2$  and a screw-pitch ratio  $t/D_b = 1.0$ . The specific dissipation profile is determined by the down-channel velocity profile, the cross-channel velocity profile, and the viscosity, as illustrated in Fig. 10. It can be seen that, for both increasing positive and negative dimensionless pressure gradients, specific dissipation

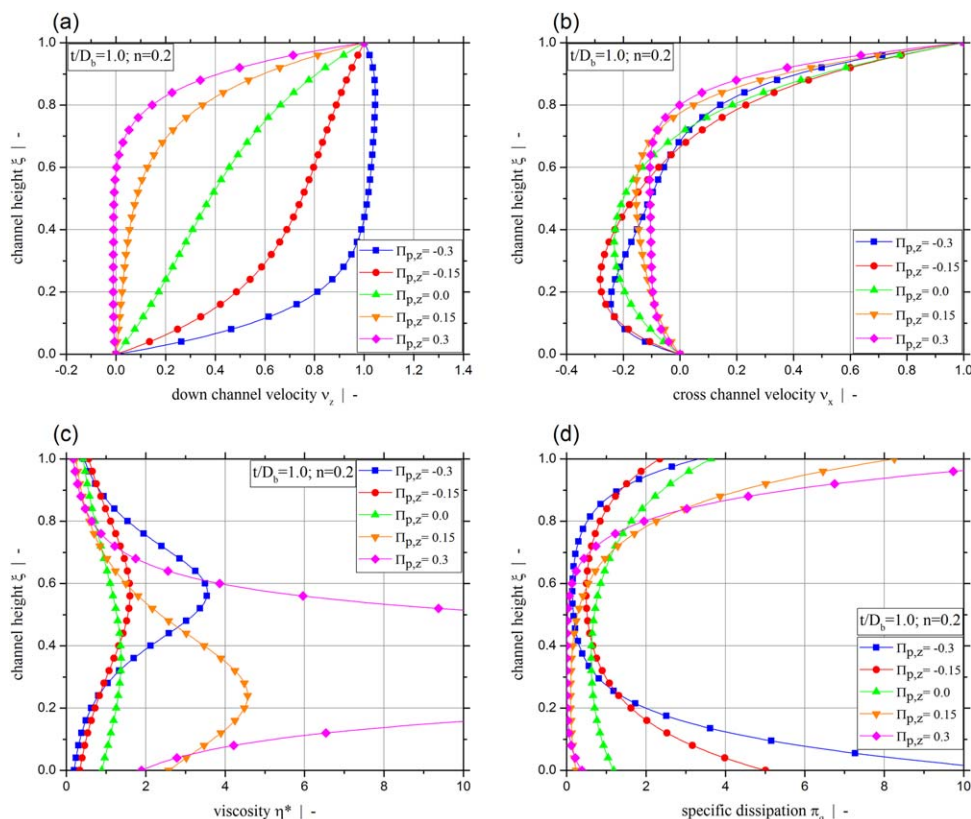


FIG. 10. Dimensionless channel height  $\xi$  versus dimensionless down-channel velocity  $v_z$  (a), dimensionless cross-channel velocity  $v_x$  (b), dimensionless viscosity  $\eta^*$  (c), and dimensionless specific dissipation  $\pi_q$  (d) for various dimensionless down-channel pressure gradients  $\Pi_{p,z}$  for  $n = 0.2$ , and  $t/D_b = 1.0$ . [Color figure can be viewed at [wileyonlinelibrary.com](https://onlinelibrary.wiley.com)]

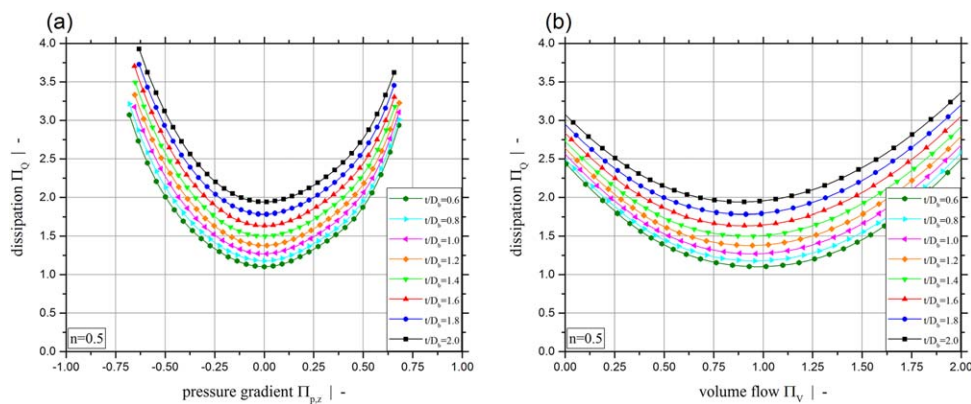


FIG. 11. Dimensionless dissipation  $\Pi_Q$  of the two-dimensional analysis for a power-law exponent  $n=0.5$  as a function of the dimensionless down-channel pressure gradient  $\Pi_{p,z}$  (a) and as a function of the dimensionless volume flow rate  $\Pi_V$  (b) for various screw-pitch ratios  $t/D_b$ . [Color figure can be viewed at wileyonlinelibrary.com]

increases. Most dissipation occurs in pressure build-up zones near the barrel surface, and in overridden zones near the screw surface.

To better show the influence of screw-pitch ratio on dimensionless dissipation, Fig. 11 plots the dimensionless dissipation  $\Pi_Q$  for a power-law exponent of  $n=0.5$  as a function of the dimensionless down-channel pressure gradient  $\Pi_{p,z}$  (Fig. 11a) and as a function of the dimensionless volume flow rate  $\Pi_V$  (Fig. 11b) for various screw-pitch ratios  $t/D_b$ . In contrast to the

throughput-pressure relationship, dimensionless dissipation also depends on the screw-pitch ratio in Newtonian fluids. With increasing screw-pitch ratio dimensionless dissipation increases significantly for both a constant dimensionless pressure gradient and a constant dimensionless throughput. This can be explained by an increase in the cross-channel flow that results in greater shearing and thus in increased viscous dissipation (see Fig. 12d). Figure 12 additionally shows the effect of the cross-channel on the down-channel velocity profile. These two velocity components

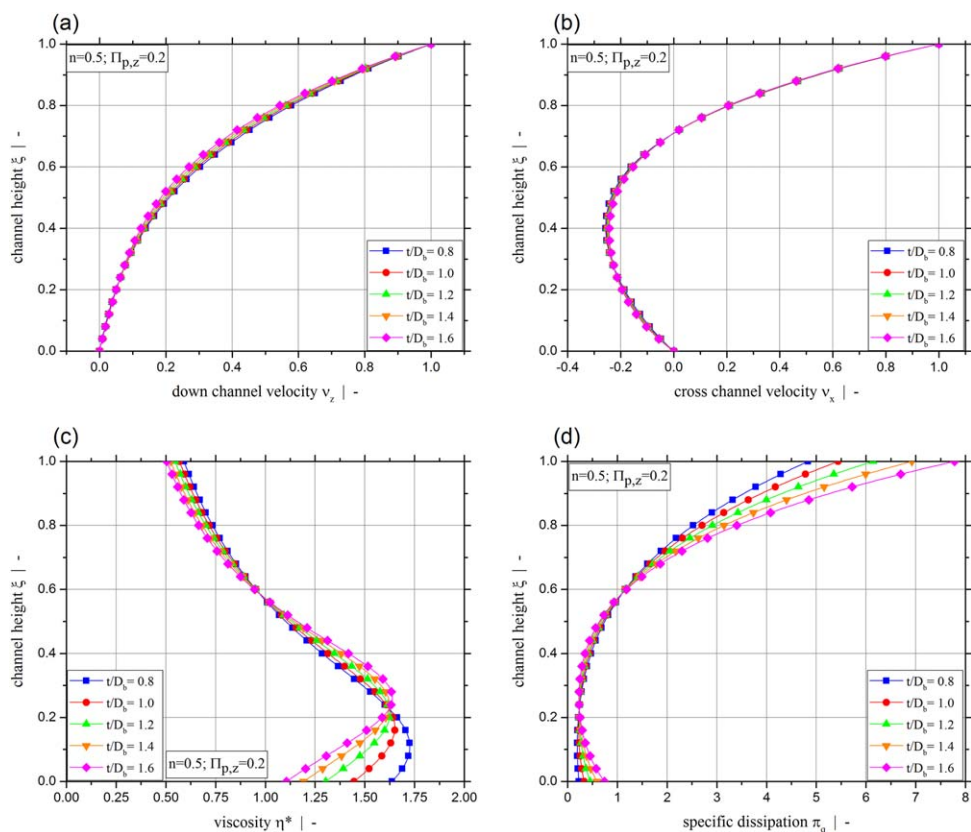


FIG. 12. Dimensionless channel height  $\xi$  versus dimensionless down-channel velocity  $v_z$  (a), dimensionless cross-channel velocity  $v_x$  (b), dimensionless viscosity  $\eta^*$  (c), and dimensionless specific dissipation  $\pi_q$  (d) for various dimensionless screw-pitch ratios  $t/D_b$  for  $n=0.5$ , and  $\Pi_{p,z}=0.2$ . [Color figure can be viewed at wileyonlinelibrary.com]

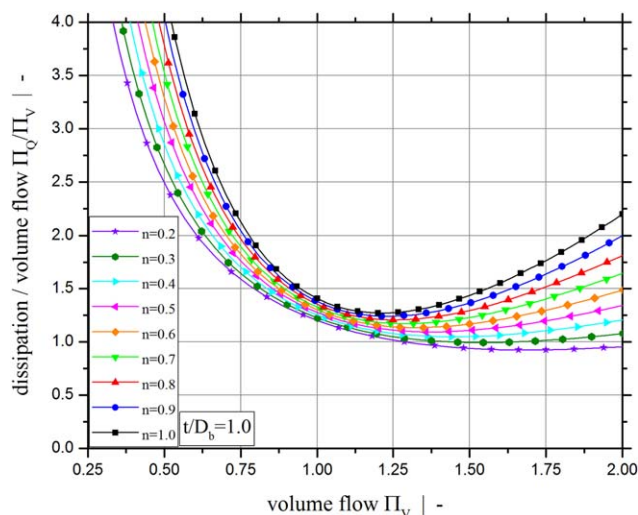


FIG. 13. Dimensionless dissipation per dimensionless throughput  $\Pi_Q/\Pi_V$  of the two-dimensional analysis for a screw-pitch of  $t/D_b=1.0$  as a function of the dimensionless flow rate  $\Pi_V$  for various power-law exponents  $n$ . [Color figure can be viewed at wileyonlinelibrary.com]

influence each other due to the shear-rate-dependent viscosity. It can also be seen that, for a moderate power-law exponent of  $n=0.5$ , the influence of screw-pitch on the velocity profiles is relatively small compared to its influence on the dissipation profile.

Another interesting quantity that gives an indication of the potential for increasing the melt temperature is dissipation per throughput. For an adiabatic extrusion process with a temperature-independent viscosity, this value would be proportional to the increase in melt temperature. To give an impression, Fig. 13 shows the dimensionless dissipation per dimensionless throughput over the dimensionless throughput for a variety of power-law exponents and a screw pitch of  $t/D_b=1.0$ . Again, it can be seen that dissipation increases with increasing power-law exponent for a constant dimensionless throughput. As previously, the minimum dimensionless dissipation occurs for pure drag flow; however, it can now be seen that the dissipation per throughput is at minimum in a slightly over-ridden melt-conveying zone. In pressure build-up zones, the dissipation per throughput increases significantly with decreasing throughput.

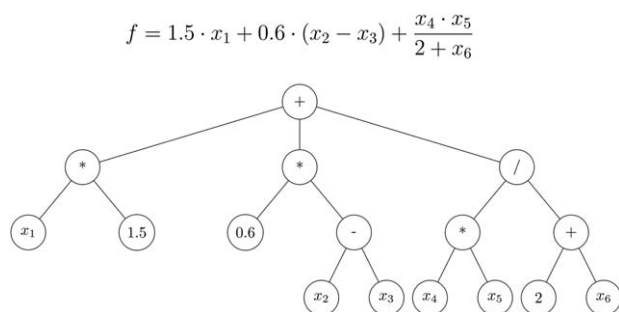


FIG. 14. Example of a symbolic regression model in mathematical notation and in parse-tree form.

TABLE 3. Independent input parameters for the symbolic regression.

One-dimensional	Two-dimensional
$\Pi_{p,z}, n$	$\Pi_{p,z}, n, t/D_b$
$\Pi_V, n$	$\Pi_V, n, t/D_b$

## ANALYTICAL APPROXIMATION

The results presented in the previous section were derived numerically by applying the theory of similarity. To avoid extensive numerical calculations, an analytical relationship is desired that mathematically describes the relationship between the characteristic influencing parameters and the target variable  $\Pi_Q$ . We used the HeuristicLab open-source software package to derive analytical approximation equations by means of symbolic regression employing genetic programming.

### Symbolic Regression - Heuristic Modeling

In general, symbolic regression based on genetic algorithms searches for a mathematical relationship between the specified independent input parameters and the dependent output parameter (target variable) without the need for predefining a specific model structure that best fits the given dataset [18]. In contrast to other common regression methods, such as linear regression and polynomial regression, where a specific model structure is assumed and only the complexity and the coefficients of the model are optimized, symbolic regression searches for a mathematical expression that best fits the input data without predefining a specific model structure. Hence, symbolic regression optimizes both model structure and model parameters simultaneously, thus continuously improving the regression model. Affenzeller et al. [29] provided a fundamental review of genetic programming and genetic algorithms. Typically, the results of a symbolic regression are given in the form of a parse tree, as shown in Fig. 14. The most important manipulations in genetic programming are crossover, mutation and selection. Crossover means that two or more different subtrees of different trees are taken and re-combined into one or more new symbolic regression trees, whereas mutation is essentially an arbitrary modification.

Solving a problem by means of genetic programming requires [18, 30]:

- a terminal set (set of input variables),
- a function set (functions used for symbolic regression, e.g., basic algebraic expressions, or trigonometric functions),
- a fitness function (quality measure, e.g., mean squared error),
- algorithm control parameters (e.g., population size, crossover, and mutation probability) and
- a termination criterion to be determined.

TABLE 4. Mathematical building blocks used for symbolic regression.

Building block	
Variables	✓
Constants	✓
Operators	+, −, *, /

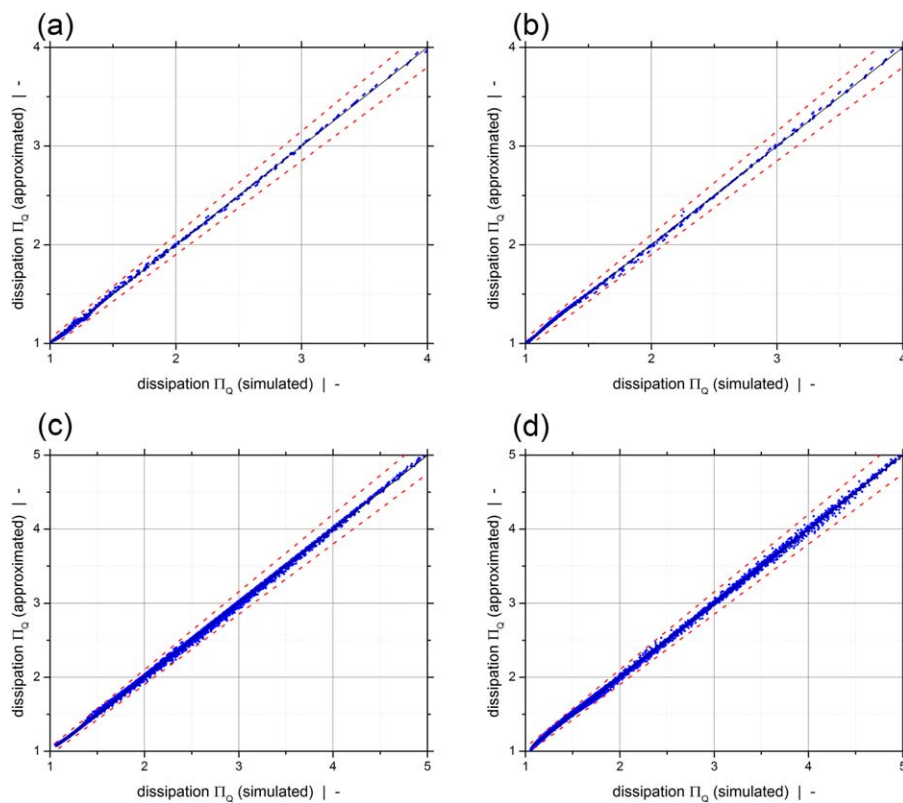


FIG. 15. Scatter plots, approximated dissipation versus simulated dissipation for all four approximations: (a)  $\Pi_Q(\Pi_{p,z}, n)$ , (b)  $\Pi_Q(\Pi_V, n)$ , (c)  $\Pi_Q(\Pi_{p,z}, n, t/D_b)$ , and (d)  $\Pi_Q(\Pi_V, n, t/D_b)$ . The dashed lines indicate the maximum relative error of 5%. [Color figure can be viewed at [wileyonlinelibrary.com](https://onlinelibrary.wiley.com)]

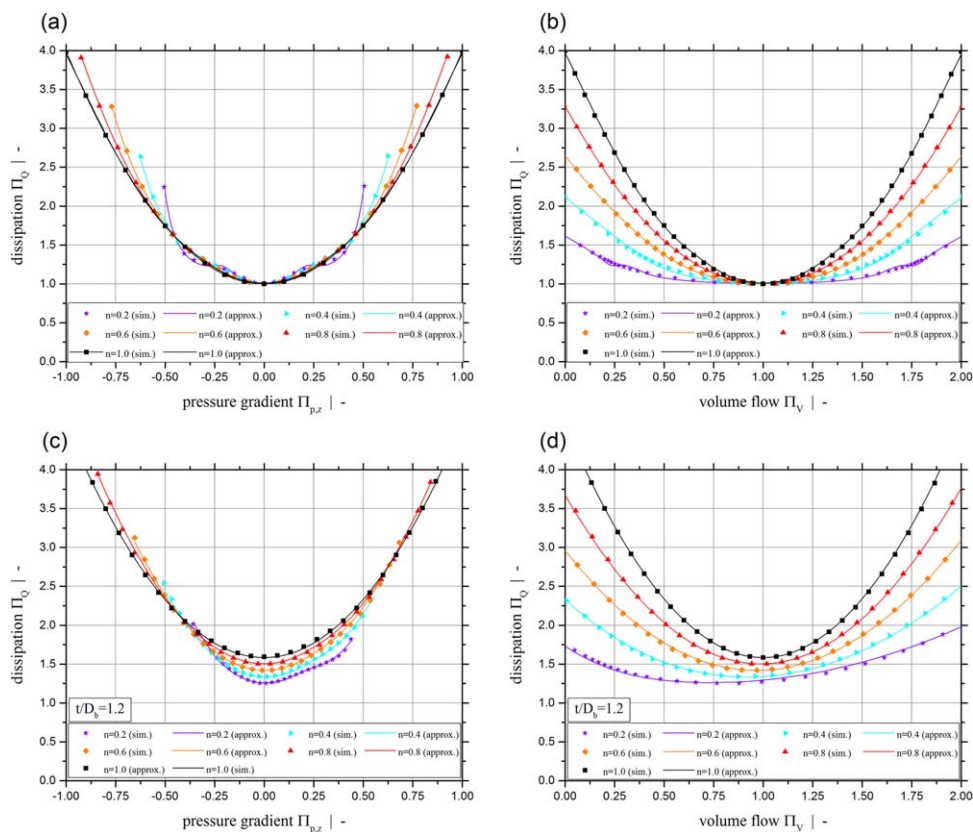


FIG. 16. Comparison of the numerical solution and the approximation for (a)  $\Pi_Q(\Pi_{p,z}, n)$ , (b)  $\Pi_Q(\Pi_V, n)$ , (c)  $\Pi_Q(\Pi_{p,z}, n, t/D_b)$  for  $t/D_b = 1.2$ , and (d)  $\Pi_Q(\Pi_V, n, t/D_b)$  for  $t/D_b = 1.2$ . [Color figure can be viewed at [wileyonlinelibrary.com](https://onlinelibrary.wiley.com)]



In total, four mathematical approximation equations are sought that describe the relationships between target variable  $\Pi_Q$  and the independent input parameters. For both the one-dimensional and two-dimensional approach two regression solutions are sought using the influencing parameters given in Table 3. A mathematical regression solution for dimensionless dissipation as a function of either the dimensionless pressure gradient  $\Pi_{p,z}$  or dimensionless throughput  $\Pi_V$  is valuable because the throughput-pressure calculation can then be performed for both a given pressure drop/increase and a given throughput.

To keep the symbolic regression model as accurate and simple as possible its mathematical building blocks (see Table 4) were constrained. Aside from the input variables and constants, only the basic arithmetic mathematical operators “addition,” “subtraction,” “multiplication,” and “division” were applied.

We used the “Pearson  $R^2$  evaluator” to optimize the symbolic regression solution. This means that for evaluating and optimizing of the heuristic solution, the coefficient of determination  $R^2$  (Eq. 59) is optimized, where  $y_i$  are the simulation values,  $\hat{y}_i$  the regression values, and  $\bar{y}$  is the mean of the simulation values. The coefficient of determination lies in the range between 0 and 1, where  $R^2=0$  means that the symbolic regression does not fit the simulation data at all, and  $R^2=1$  means that the symbolic regression fits the simulation data completely [29].

$$R^2 = 1 - \frac{\sum_{i=1}^n (y_i - \hat{y}_i)^2}{\sum_{i=1}^n (y_i - \bar{y})^2}. \quad (59)$$

### Symbolic Regression Results

For each of the approaches (one- and two-dimensional), two symbolic regression equations were derived that approximated the 729 and 8,784 numerically derived design points, respectively. Equation 60 predicts the one-dimensional dimensionless dissipation as a function of  $\Pi_Q = f(\Pi_{p,z}, n)$ , and Eq. 61 predicts the one-dimensional dissipation as a function of  $\Pi_Q = f(\Pi_V, n)$ , where  $A_1$  to  $A_5$  and  $B_1$  to  $B_3$  are sub-functions containing 17 and 12 constants, respectively (see Appendix for the sub-functions and the rounded values of the constants: Table 5 for  $\Pi_Q = f(\Pi_{p,z}, n)$ , and Table 6 for  $\Pi_Q = f(\Pi_V, n)$ ).

$$\Pi_Q(\Pi_{p,z}, n) = A_1 + \frac{A_2}{A_3 + A_4 + A_5}. \quad (60)$$

$$\Pi_Q(\Pi_V, n) = B_1 + \frac{B_2}{B_3}. \quad (61)$$

Equation 62 predicts the two-dimensional dissipation as a function of  $\Pi_Q = f(\Pi_{p,z}, n, t/D_b)$ , and Eq. 63 predicts the two-dimensional dissipation as a function of  $\Pi_Q = f(\Pi_V, n, t/D_b)$ , where  $C_1$  to  $C_6$  and  $D_1$  to  $D_5$  are sub-functions containing 22 and 20 constants, respectively [see Appendix for the sub-functions and the rounded values of the constants: Table 7 for  $\Pi_Q = f(\Pi_{p,z}, n, t/D_b)$ , and Table 9 for  $\Pi_Q = f(\Pi_V, n, t/D_b)$ ].

$$\Pi_Q(\Pi_{p,z}, n, t/D_b) = C_1 + C_2 + C_3 + \frac{C_4 + C_5}{C_6}. \quad (62)$$

$$\Pi_Q(\Pi_V, n, t/D_b) = D_1 + D_2 (D_3 - D_4 + D_5). \quad (63)$$

Based on these approximation equations, the viscous dissipation can be predicted for both pressure-generating and overridden melt-conveying zones. Prediction is possible either for a given pressure gradient or for a given throughput without the need for time-consuming and computationally expensive numerical calculations. In Eqs. 62 and 63, the cross-channel flow is also taken into account. It has a significant impact on viscous dissipation, as shown above. All four analytical approximations show high accuracy, despite a relatively simple model and a moderate number of coefficients. Model accuracy was validated by means of an error analysis. In addition to the coefficient of determination  $R^2$ , we evaluated the mean absolute error (MAE), the maximum absolute error, the mean relative error (MRE), and the maximum relative error. The detailed results of the error analysis are given in Table 8. The coefficient of determination is approximately  $R^2=0.9995$ , the MAE is in the range of  $\text{MAE}=0.01198 \dots 0.0141$ , and the MRE is in the range of  $\text{MRE}=0.641\% \dots 0.824\%$ , which indicates a very close analytical approximation of the numerical results. Furthermore, the scatter plots in Fig. 15 show the normalized approximation versus the numerical results, where the approximation Equations were applied for all simulation setups. It can be seen that all values are within  $\pm 5\%$ .

Note that application of the presented models is limited to the range of the input parameters used in the parametric study. This means that, were the input parameters outside these limits, the analytical approximation models would no longer be valid and further numerical calculations would be necessary. However, the broad scope of the comprehensive parametric study covers almost all polymer melts and screw designs used in industry.

Comparisons of simulation results and approximated solutions using the exact values of the constants for the heuristic model are given in Fig. 16. For the two-dimensional model, the comparison is shown for a constant screw pitch of  $t/D_b=1.2$  for various power-law exponents. It can be seen that all four models fit the simulation results very accurately.

### CONCLUSIONS

We developed four analytical relationships for predicting viscous dissipation in single-screw extrusion, taking into account both non-Newtonian fluid behavior and the screw pitch. The non-Newtonian fluid behavior is considered using the power-law model. Based on a dimensional analysis, three independent input parameters were identified that describe the non-Newtonian flow of a two-dimensional extruder flow: the dimensionless pressure gradient  $\Pi_{p,z}$ , the power-law exponent  $n$ , and the screw-pitch ratio  $t/D_b$ . Additionally, we identified a second set of three independent input parameters that describe the flow: the dimensionless throughput  $\Pi_V$ , the power-law exponent  $n$ , and the screw-pitch ratio  $t/D_b$ . We have presented four heuristic models of viscous dissipation based on both sets of independent input parameters for one- and two-dimensional flows. The analytical approximation equations were derived by a heuristic approximation method using symbolic regression based on genetic programming approximating numerically derived results. The presented models accurately approximate the numerical solutions of a comprehensive parametric study with 729 and

8,784 independent design points defined by applying the theory of similarity for the one- and the two-dimensional case, respectively. The accuracy of our heuristic models was demonstrated by an error analysis, which yielded a coefficient of determination of approximately  $R^2=0.9995$ , a  $MRE \leq 0.824\%$  and a maximum relative error  $RE_{\max} \leq 5\%$  for all four models.

Our models enable fast and stable prediction of the viscous dissipation of the two-dimensional flow in the melt-conveying zone of single-screw extruders without the need for numerical simulations. Since viscous dissipation is mainly responsible for the increase in melt temperature, our models provide an excellent basis for calculating the axial melt temperature development. Considering the temperature-dependent viscosity, the non-isothermal throughput can be calculated on the basis of the axial melt temperature profile derived. Since in narrow screw channels the screw flights also have an impact on viscous dissipation, we are currently extending our model to address three-dimensional flow.

## NOMENCLATURE

$A_1 - A_5$	Sub-functions
$B_1 - B_3$	Sub-functions
$C_1 - C_6$	Sub-functions
$D_1 - D_6$	Sub-functions
$a_{00} - a_{16}$	Constants
$b_{00} - b_{12}$	Constants
$c_{00} - c_{21}$	Constants
$d_{00} - d_{19}$	Constants
$\mathbf{A}_z, \mathbf{A}_x$	FDM matrices
$\mathbf{v}_z, \mathbf{v}_x$	FDM node velocity vectors
$\mathbf{p}_z, \mathbf{p}_x$	FDM node pressure vectors
$D_b$	Barrel diameter
$h$	Channel height
$w$	Channel width
$i$	Number of parallel screw channels
$\delta$	Flight clearance
$\varphi_b$	Helix angle at outer diameter
$v_b$	Barrel velocity
$v_{b,z}$	Barrel velocity in x-direction
$v_{b,x}$	Barrel velocity in y-direction
$x, y, z$	Spatial coordinates
$v_x, v_y, v_z$	Velocity components
$t$	Screw pitch
$N$	Screw speed
$\eta$	Viscosity
$\dot{\gamma}$	Shear rate
$K$	Consistency
$n$	Power-law exponent
$\rho$	Melt density
$p$	Hydrostatic pressure
$\mathbf{D}$	Rate-of-deformation tensor
$\tau$	Viscous stress tensor
$\tau_{ij}$	Components of the stress tensor
$g$	Gravity
$Re$	Reynolds number
$\dot{V}$	Volumetric flow rate
$\dot{q}_{diss}$	Specific viscous dissipation
$\dot{Q}_{diss}$	Viscous dissipation
$\xi$	Dimensionless coordinate in up-channel direction

$v_z, v_x$	Dimensionless velocities
$\dot{\gamma}^*$	Dimensionless shear rate
$\eta^*$	Dimensionless viscosity
$\Pi_{p,z}, \Pi_{p,x}$	Dimensionless pressure gradients
$\Pi_V$	Dimensionless volumetric flow rate
$\pi_Q$	Dimensionless specific viscous dissipation
$\Pi_Q$	Dimensionless viscous dissipation

## ACKNOWLEDGMENTS

This work was supported by the Austrian COMET K2 program of the Linz Center of Mechatronics (LCM), and was funded by the Austrian federal government and the federal state of Upper Austria.

## APPENDIX

Definitions of  $\mathbf{A}_z$ ,  $\mathbf{v}_z$ , and  $\mathbf{p}_z$ : the coefficients for the finite difference matrix, the vector with the unknown velocities, and the load vector in the down-channel direction, respectively. Note that the indices  $i$  and  $j$  run from  $1 \dots N$ , where  $N$  is the number of equidistant divisions.

$$\begin{aligned} A_{z,ij} &= -\left(\eta_{i+3/2}^* + \eta_{i+1/2}^*\right) & \dots & j=i \\ A_{z,ij} &= \eta_{j+1/2}^* & \dots & j=i+1 \\ A_{z,ij} &= \eta_{j-1/2}^* & \dots & j=i-1 \\ A_{z,ij} &= 0 & \dots & \text{else} \end{aligned} \quad (\text{A1})$$

$$v_{z,i} = v_{z,i+1} \quad (\text{A2})$$

$$\begin{aligned} p_{z,i} &= 6 \Pi_{p,z} \Delta \xi^2 - v_{z,1} \eta_{1/2}^* & \dots & i=1 \\ p_{z,i} &= 6 \Pi_{p,z} \Delta \xi^2 - v_{z,N+1} \eta_{N+1/2}^* & \dots & i=N-1 \\ p_{z,i} &= 6 \Pi_{p,z} \Delta \xi^2 & \dots & \text{else} \end{aligned} \quad (\text{A3})$$

Definitions of  $\mathbf{A}_x$ ,  $\mathbf{v}_x$ , and  $\mathbf{p}_x$ : the coefficients for the finite difference matrix, the vector with the unknown velocities including the cross-channel pressure gradient, and the load vector in the cross-channel direction, respectively. Note that the indices  $i$  and  $j$  run from  $1 \dots N+1$ , where  $N$  is the number of equidistant divisions.

TABLE 5. Rounded values of the constants for  $\Pi_Q = \Pi_Q(\Pi_{p,z}, n)$ .

Constant	Value	Constant	Value	Constant	Value
$a_{00}$	1.0098	$a_{06}$	-133.88	$a_{12}$	13.539
$a_{01}$	0.028280	$a_{07}$	-247.34	$a_{13}$	-2.4645
$a_{02}$	2.1025	$a_{08}$	441.92	$a_{14}$	88.383
$a_{03}$	8.2382	$a_{09}$	-11.414	$a_{15}$	-1092.7
$a_{04}$	-1.1715	$a_{10}$	12.737	$a_{16}$	-0.70578
$a_{05}$	-1.8456	$a_{11}$	-4.2800		

TABLE 6. Rounded values of the constants for  $\Pi_Q = \Pi_Q(\Pi_V, n)$ .

Constant	Value	Constant	Value	Constant	Value
$b_{00}$	0.98667	$b_{05}$	65.113	$b_{10}$	-0.056002
$b_{01}$	0.31119	$b_{06}$	0.63600	$b_{11}$	-1.5981
$b_{02}$	0.15900	$b_{07}$	-0.54151	$b_{12}$	15.562
$b_{03}$	-0.13540	$b_{08}$	-0.11586		
$b_{04}$	-74.947	$b_{09}$	0.23655		

$$\begin{aligned}
 A_{x,ij} &= 0 & \dots & i=j=N \\
 A_{x,ij} &= 2/3 & \dots & i=N, j=1, 3, 5, \dots \\
 A_{x,ij} &= 1/3 & \dots & i=N, j=2, 4, 6, \dots \\
 A_{x,ij} &= -\frac{6\Delta\xi^2}{\tan(\varphi_b)} & \dots & i=1 \dots N-1, j=N
 \end{aligned} \quad (A4)$$

$$\begin{aligned}
 A_{x,ij} &= -\left(\eta_{i+3/2}^* + \eta_{i+1/2}^*\right) & \dots & j=i < N \\
 A_{x,ij} &= \eta_{j+1/2}^* & \dots & j=i+1, i < N, j < N \\
 A_{x,ij} &= \eta_{j-1/2}^* & \dots & j=i-1, i < N, j < N \\
 A_{x,ij} &= 0 & \dots & \text{else} \\
 v_{z,i} &= v_{z,i+1} & \dots & i=1 \dots N-1 \\
 v_{z,i} &= \Pi_{p,x} & \dots & i=N \\
 p_{z,i} &= -v_{x,1} \eta_{1/2}^* & \dots & i=1 \\
 p_{z,i} &= -v_{x,N+1} \eta_{N+1/2}^* & \dots & i=N-1 \\
 p_{z,i} &= -\frac{1}{6}(v_{x,1} + v_{x,2}) & \dots & i=N \\
 p_{z,i} &= 0 & \dots & \text{else}
 \end{aligned} \quad (A5)$$

Sub-functions of Eq. 60:  $\Pi_Q = \Pi_Q(\Pi_{p,z}, n)$

TABLE 7. Rounded values of the constants for  $\Pi_Q = \Pi_Q(\Pi_{p,z}, n, t/D_b)$ .

Constant	Value	Constant	Value	Constant	Value
$c_{00}$	0.79465	$c_{08}$	-0.10794	$c_{16}$	0.0022366
$c_{01}$	-0.011918	$c_{09}$	0.029996	$c_{17}$	0.41981
$c_{02}$	4.0135	$c_{10}$	0.18962	$c_{18}$	1.0306
$c_{03}$	-0.99728	$c_{11}$	0.31205	$c_{19}$	0.034865
$c_{04}$	0.023509	$c_{12}$	0.0070964	$c_{20}$	-0.084116
$c_{05}$	0.23613	$c_{13}$	-3.1825	$c_{21}$	365.90
$c_{06}$	0.061547	$c_{14}$	0.10251		
$c_{07}$	0.063283	$c_{15}$	0.029155		

TABLE 8. Quality measures for the heuristic approximation equations.

Quality measure	Unit	$\Pi_Q(\Pi_{p,z}, n)$	$\Pi_Q(\Pi_V, n)$	$\Pi_Q(\Pi_{p,z}, n, t/D_b)$	$\Pi_Q(\Pi_V, n, t/D_b)$
Pearson $R^2$	—	0.99957	0.99949	0.99938	0.99950
Mean abs. error	—	0.01198	0.01219	0.0138	0.0141
Max. abs. error	—	0.0479	0.07769	0.1163	0.1217
Mean rel. error	%	0.811	0.824	0.641	0.696
Max. rel. error	%	3.230	3.513	5.026	4.412

$$A_1 = a_{00} \quad (A7)$$

$$A_2 = \Pi_{p,z}^2 (a_{01} \Pi_{p,z} n + a_{02} n^2 + a_{03} n + a_{04}) \quad (A8)$$

$$A_3 = a_{05} \Pi_{p,z}^2 \quad (A9)$$

$$A_4 = \frac{n (a_{06} n^2 + a_{07} n + a_{08})}{(a_{09} n + a_{10}) (\Pi_{p,z}^2 + a_{12})} \quad (A10)$$

$$A_5 = \frac{n}{a_{13} n + \Pi_{p,z}^4 (a_{14} n + a_{15} \Pi_{p,z}^2 + a_{16})} \quad (A11)$$

Sub-functions of Eq. 61:  $\Pi_Q = \Pi_Q(\Pi_V, n)$

$$B_1 = b_{00} \quad (A12)$$

$$B_2 = \left( \frac{b_{01} n^2}{b_{02} \Pi_V + b_{03}} + b_{04} n + b_{05} n \Pi_V \right) (b_{06} \Pi_V + b_{07}) \quad (A13)$$

$$B_3 = \frac{b_{08} \Pi_V^2 + b_{09} \Pi_V + b_{10}}{n^2} + b_{11} n^2 + b_{12} \quad (A14)$$

Sub-functions of Eq. 62:  $\Pi_Q = \Pi_Q(\Pi_{p,z}, n, t/D_b)$

$$C_1 = c_{00} + c_{01} \Pi_{p,z} + c_{02} \Pi_{p,z}^2 + c_{03} n^2 \Pi_{p,z}^2 + c_{04} n^2 \Pi_{p,z}^3 + c_{05} t/D_b \quad (A15)$$

$$C_2 = c_{06} t/D_b \Pi_{p,z} + c_{07} n^2 \Pi_{p,z} t/D_b \quad (A16)$$

$$C_3 = \frac{\Pi_{p,z} t/D_b (c_{08} + c_{09} \Pi_{p,z})}{n + c_{10} \Pi_{p,z}} + c_{11} n t/D_b^2 \quad (A17)$$

$$C_4 = c_{12} + c_{13} t/D_b \Pi_{p,z}^5 + c_{14} \Pi_{p,z} t/D_b^2 \quad (A18)$$

$$C_5 = n (c_{15} + c_{16} \Pi_{p,z}^2 + c_{17} \Pi_{p,z}^3 + c_{18} \Pi_{p,z}^4 + c_{19} t/D_b + c_{20} \Pi_{p,z} t/D_b^2) \quad (A19)$$

$$C_6 = n t/D_b + c_{21} t/D_b \Pi_{p,z}^6 \quad (A20)$$

Sub-functions of Eq. 63:  $\Pi_Q = \Pi_Q(\Pi_V, n, t/D_b)$

$$D_1 = d_{00} \quad (A21)$$

$$D_2 = \frac{n}{1 + d_{19} n^3} \quad (A22)$$

$$D_3 = t/D_b \left( d_{01} \Pi_V + d_{02} + \frac{d_{03}}{d_{04} + n \Pi_V} + d_{05} t/D_b + d_{06} t/D_b^2 \right) \quad (A23)$$

$$D_4 = \frac{d_{07} + d_{08} n + d_{09} \frac{\Pi_V}{n} - \frac{d_{10} n}{d_{11} + t/D_b}}{n + d_{12} \Pi_V^2} \quad (A24)$$

TABLE 9. Rounded values of the constants for  $\Pi_Q = \Pi_Q(\Pi_V, n, t/D_b)$ .

Constant	Value	Constant	Value	Constant	Value
$d_{00}$	1.7121	$d_{07}$	0.57647	$d_{14}$	2.4540
$d_{01}$	-0.29081	$d_{08}$	10.787	$d_{15}$	-0.069668
$d_{02}$	0.050859	$d_{09}$	0.097780	$d_{16}$	-13.538
$d_{03}$	14.699	$d_{10}$	112.70	$d_{17}$	-156.44
$d_{04}$	9.5324	$d_{11}$	8.5365	$d_{18}$	0.014717
$d_{05}$	0.15916	$d_{12}$	0.44378	$d_{19}$	-0.16476
$d_{06}$	0.020228	$d_{13}$	-4.2297		

$$D_5 = \Pi_V \left[ d_{13} + d_{14} \Pi_V + d_{15} \left( n + \frac{d_{16} \Pi_V^2}{d_{17} + n} \right)^{-1} \left( n + d_{18} \frac{t/D_b^4}{n} \right)^{-1} \right] \quad (A25)$$

## REFERENCES

1. H.S. Rowell, and D. Finlayson, *Engineering*, **114**, 606 (1922).
2. H.S. Rowell, and D. Finlayson, *Engineering*, **126**, 249 (1928).
3. J.F. Carley, R.S. Mallouk, and J.M. McKelvey, *Ind. Eng. Chem.*, **45**, 974 (1953).
4. W.D. Mohr, R.L. Saxton, and C.H. Jepson, *Ind. Eng. Chem.*, **49**, 1857 (1957).
5. W.D. Mohr, and R.S. Mallouk, *Ind. Eng. Chem.*, **51**, 765 (1959).
6. C. Rauwendaal, *Polymer Extrusion*, 5th ed., Carl Hanser Verlag, Munich (2014).
7. Z. Rotem, and R. Shinnar, *Chem. Eng. Sci.*, **15**, 130 (1961).
8. R.M. Griffith, *Ind. Eng. Chem. Fund.*, **1**, 180 (1962).
9. H.J. Zamodits, and J.R.A. Pearson, *J. Rheol.*, **13**, 357 (1969).
10. M.L. Booy, *Polym. Eng. Sci.*, **21**, 93 (1981).
11. Z. Tadmor, and I. Klein, *Engineering Principles of Plasticating Extrusion*, Van Nostrand Reinhold Company, New York (1970).
12. C. Rauwendaal, *Polym. Eng. Sci.*, **26**, 1240 (1986).
13. H. Potente, *Rheol. Acta*, **22**, 387 (1983).
14. J. L. White, and H. Potente, *Screw Extrusion: Science and Technology*, Carl Hanser Verlag, Munich (2003).
15. S. Pachner, B. Löw-Baselli, M. Affenzeller, and J. Miethlinger, *Int. Polym. Process*, **32**, 209 (2017).
16. C. Marschik, W. Roland, B. Löw-Baselli, and J. Miethlinger, *SPE ANTEC Tech. Pap.*, **1125** (2017).
17. C. Marschik, W. Roland, B. Löw-Baselli, and J. Miethlinger, *J. Non. Newt. Fluid Mech.*, **248**, 27 (2017).
18. J. R. Koza, *Genetic programming: On the Programming of Computers by Means of Natural Selection*, The MIT Press, Cambridge, Massachusetts (1992).
19. G. Bramerdorfer, S.M. Winkler, M. Kommenda, G. Weidenholzer, S. Silber, G. Kronberger, M. Affenzeller, and W. Amrhein, *IEEE Trans. Ind. Electron.*, **61**, 6454 (2014).
20. E. Lughofer, G. Kronberger, M. Kommenda, S. Saminger-Platz, A. Promberger, F. Nickel, S. Winkler, and M. Affenzeller, *Proceedings of the 8th International Joint Conference Computational Intelligence*. Porto, **51** (2016).
21. H. Potente, and C. Obermann, *Int. Polym. Process*, **14**, 21 (1999).
22. G.A. Campbell, C. Wang, H. Cheng, M. Bullwinkel, and M.A. te-Riele, *Int. Polym. Process*, **16**, 323 (2001).
23. S.J. Derezinski, *J. Plast. Film Sheeting*, **3**, 274 (1987).
24. S. J. Derezinski, *SPE ANTEC Tech. Pap.*, **417** (1996).
25. S. J. Derezinski, *SPE ANTEC Tech. Pap.*, (2013).
26. W. Roland, and J. Miethlinger, *SPE ANTEC Tech. Pap.*, **1005** (2017).
27. Z. Tadmor, and C. G. Gogos, *Principles of Polymer Processing*, 2nd ed., Wiley, New York (2006).
28. H. P. Langtangen, and G. K. Pedersen, *Scaling of Differential Equations*, Springer, Switzerland (2016).
29. M. Affenzeller, S. Wagner, S. Winkler, and A. Beham, *Genetic Algorithms and Genetic Programming: Modern Concepts and Practical Applications*, Chapman & Hall/CRC Press, London (2009).
30. M. J. Willis, H. G. Hidden, P. Marenbach, B. McKay, and G. A. Montague, *GALESIA 97*, Glasgow, UK, **314** (1997).